ARTICLE

Small Multifunctional Nanoclusters (Nanoroses) for Targeted Cellular Imaging and Therapy

Li Leo Ma,[†,‡] Marc D. Feldman,[‡,§,*] Jasmine M. Tam,[†] Amit S. Paranjape,[∥] Kiran K. Cheruku,[§] Timothy A. Larson,[∥,#] Justina O. Tam,[∥,#] Davis R. Ingram,[†] Vidia Paramita,[†] Joseph W. Villard,[§] James T. Jenkins,[§] Tianyi Wang,[∥] Geoffrey D. Clarke,[§] Reto Asmis,[¶] Konstantin Sokolov,[∥,⊥,#] Bysani Chandrasekar,[‡,§] Thomas E. Milner,[∥,#] and Keith P. Johnston[†,#,*]

[†]Department of Chemical Engineering, University of Texas at Austin, Austin, Texas 78712, [‡]South Texas Veterans Affairs Hospital System, San Antonio, Texas 78229, [§]Division of Cardiology, Department of Medicine, University of Texas Health Science Center at San Antonio, San Antonio, Texas 78229, [∥]Department of Biomedical Engineering, University of Texas at Austin, Austin, Texas 78712, [¶]Office of the Dean, School of Health Professions, University of Texas Health Science Center at San Antonio, San Antonio, Texas 78229, [⊥]Departments of Biomedical Engineering and Imaging Physics, M.D. Anderson Cancer Center, Houston, Texas 77030, and [#]Center for Nano and Molecular Science and Technology, University of Texas at Austin, Austin, Texas 78712

ABSTRACT The ability of 20−50 nm nanoparticles to target and modulate the biology of specific types of cells will enable major advancements in cellular imaging and therapy in cancer and atherosclerosis. A key challenge is to load an extremely high degree of targeting, imaging, and therapeutic functionality into small, yet stable particles. Herein we report ~30 nm stable uniformly sized near-infrared (NIR) active, superparamagnetic nanoclusters formed by kinetically controlled self-assembly of gold-coated iron oxide nanoparticles. The controlled assembly of nanocomposite particles into clusters with small primary particle spacings produces collective responses of the electrons that shift the absorbance into the NIR region. The nanoclusters of ~70 iron oxide primary particles with thin gold coatings display intense NIR (700−850 nm) absorbance with a cross section of $\sim 10^{-14}$ m^2. Because of the thin gold shells with an average thickness of only 2 nm, the r_2 spin−spin magnetic relaxivity is 219 mM^{-1} s^{-1}, an order of magnitude larger than observed for typical iron oxide particles with thicker gold shells. Despite only 12% by weight polymeric stabilizer, the particle size and NIR absorbance change very little in deionized water over 8 months. High uptake of the nanoclusters by macrophages is facilitated by the dextran coating, producing intense NIR contrast in dark field and hyperspectral microscopy, both in cell culture and an *in vivo* rabbit model of atherosclerosis. Small nanoclusters with optical, magnetic, and therapeutic functionality, designed by assembly of nanoparticle building blocks, offer broad opportunities for targeted cellular imaging, therapy, and combined imaging and therapy.

KEYWORDS: gold · iron oxide · nanocluster · near-infrared · macrophage targeted imaging · MRI · atherosclerosis · cancer

*Address correspondence to kpj@che.utexas.edu, FELDMANM@uthscsa.edu.

Received for review May 1, 2009 and accepted August 15, 2009.

Published online August 27, 2009. 10.1021/nn900440e CCC: $40.75

Clinical imaging and/or therapy with multifunctional nanoparticles that target specific types of cells has the potential to transform health care in cancer, atherosclerosis, and other diseases. When the nanoparticle diameters are reduced to 20−50 nm, the biological pathways in targeted cells can undergo profound changes.[1−5] Small nanoparticles, the size of small viruses, permeate barriers more rapidly including cell membranes and leaky vasculature in cancers. The efficacy of vaccines may be enhanced with ultrasmall 20 nm nanoparticles that can diffuse to the lymph nodes to target resident dendritic cells.[3] Multifunctional ultrasmall paramagnetic iron oxide (USPIO) particles (~30 nm) have been designed to detect and deliver chemotherapeutic agents directly into prostate cancer cells.[4] Antibody-functionalized spherical gold particles target membrane receptors much more efficiently and modulate a variety of cell functions including cell death, as the size is reduced to 40−50 nm.[1,2] Finally, prolonged circulation in the bloodstream (slow clearance by the liver and spleen) for small nanoparticles facilitates magnetic resonance imaging (MRI) contrast for imaging atherosclerosis and imaging of lymph nodal metastases in cancer.[5,6]

New opportunities in cellular optical imaging and therapy in intact tissues have been spawned by nanoparticles including gold nanoshells, nanorods, and nanocages with absorbances 10^6-fold those of organic dyes.[7−12] For these particle geometries, the surface plasmon resonance (SPR) peak of gold shifts to the NIR region (700 and 850 nm) where soft tissue, hemoglobin, and water absorb weakly. Alternatively, gold nanospheres bioconjugated with antibodies have been assembled by cancer receptors to form NIR-active gold aggregates.[13,14] Multifunctional imaging further provides complementary anatomic, functional, and molecular information at the cellular level needed to ad-

vance therapy. For example, the location of iron oxide nanoparticles may be imaged with MRI *in vivo* while simultaneously detecting enzymatic activity in lymph nodes with NIR fluorescence upon subcutaneous injection.[15] Furthermore, multifunctional nanoparticles may be utilized for combined optical/MRI molecular imaging and photothermal therapy of cancer cells and for molecular-specific optical image contrast enhancement using magnetic modulation.[16,17]

A major challenge in nanotechnology and nanomedicine is to devise robust and broadly applicable synthetic strategies to pack sufficient multifunctionality into nanoparticles smaller than ~50 nm. The high surface energy of the nanoparticles makes it challenging to control the geometry and composition and, furthermore, to maintain the structure and functional properties in physiological media or *in vivo*. The shapes and compositions of nanoparticles may be guided during condensation of atoms by selectively favoring growth of particular crystal facets to produce spheres, rods, wires, discs, cages, core−shell structures, and many other shapes.[8,10,12,18] A less common yet highly adaptable approach is to assemble ultrasmall spherical nanoparticles as the primary building blocks, rather than atoms, into 1D, 2D, and 3D inorganic/organic nanocluster composites.[19−22] The size and shape of 3D composite nanoclusters have been controlled with block copolymer templates, DNA, proteins, and viruses, primarily for the design of sensing and memory devices.[20] However, the sizes of the clusters have been well above 50 nm in nearly all cases, or the degree of functionality has been limited because of the need for a large amount of templating and stabilizing agents. These agents have been required to control particle growth and to provide stability.

Herein, we demonstrate that primary iron oxide nanoparticles with thin gold coatings may be assembled into very stable ~30 nm nanoclusters with intense functionality, despite only a small amount of polymeric stabilizers. Unlike most previous studies of 3D clusters, the nanoparticle building block incorporates two inorganic materials, iron oxide and gold, rather than one, to provide multifunctionality. The nanoclusters composed of ~70 iron primary particles display intense NIR (700−850 nm) absorbance and r_2 magnetic relaxivity (>200 mM^{-1} s^{-1}) in solution and strong optical contrast in targeted macrophages. The small average size and relatively low polydispersity of the nanoclusters are achieved by kinetic control of self-assembly, as a function of the iron oxide nanoparticle concentration and gold: iron oxide ratio, in the presence of dextran stabilizer. The intense optical and magnetic properties of the nanoclusters far exceed the values of the constituents.[23] The intense NIR absorbance is described in terms of the close proximity of the thin and asymmetric gold coatings on the primary nanoparticles. Sufficiently small spacing between the primary particles needed for the enhanced optical and magnetic properties is favored by the small concentration of dextran stabilizer on the starting primary iron oxide particles. The small size of the nanoclusters and the dextran surface coating are shown to facilitate high uptake by macrophages, which contain dextran receptors.[6] The high uptake and intense NIR absorbance are shown to provide high NIR contrast in dark field and hyperspectral microscopy, both in cell culture and an *in vivo* rabbit model of atherosclerosis. These properties are also utilized for photothermal destruction of nanocluster-laden macrophages.

RESULTS AND DISCUSSION

Synthesis, Structure, and Stability. Nanoclusters were formed by the reduction of $HAuCl_4$ onto the surfaces of 5 nm iron oxide nanoparticles with hydroxylamine as a seeding agent. We will call these particular particles "nanoroses" to distinguish them from more general types of nanoclusters and also to emphasize their intense properties, analogous to a rose's vibrant color.[20] The hydroxylamine adsorbs on the iron oxide particle surface and favors selective formation of gold on the iron oxide surface rather than in bulk solution.[24] Previously, ~60 nm Au-coated magnetic iron oxide nanoparticles without NIR absorbance were formed with a molar Au/Fe precursor ratio of 2:1 after the first iteration.[24] In our study, a much smaller Au/Fe ratio of 1:10 by mole after all of the iterations led to much thinner gold domains. The dextran molecules on the iron oxide surface helped prevent the gold domains from growing too thick during reduction. The reaction resulted in ~30 nm relatively open clusters composed of much smaller primary particle domains. The primary domains are more easily discerned near the periphery in the TEM images (Figure 1a) but are somewhat masked toward the center, where the electrons pass through a much thicker cross section. Because the gold shells are darker than the iron oxide cores in the TEM, and the cluster geometry is rather complex, direct observation of the shells is infeasible.[25] The thickness of the gold shells may be estimated by subtracting the known 5 nm diameter of the iron oxide cores (Figure S1 in the Supporting Information) from the size of the ~7−10 nm primary domains, as has been done previously.[25] The resulting shell thickness is ~1 to 2.5 nm, and from the nonspherical shape of the primary domains, it appears to vary over the surface of a given iron oxide core, as observed for "nanoeggs" with asymmetric egg whites.[26]

The gold coatings on iron oxide cores increase the attractive van der Waals forces between particles, given the much larger Hamaker constant for Au *versus* iron oxide. The balance of these attractive forces and the steric stabilization provided by dextran, along with the iron oxide and gold precursor concentrations, resulted in

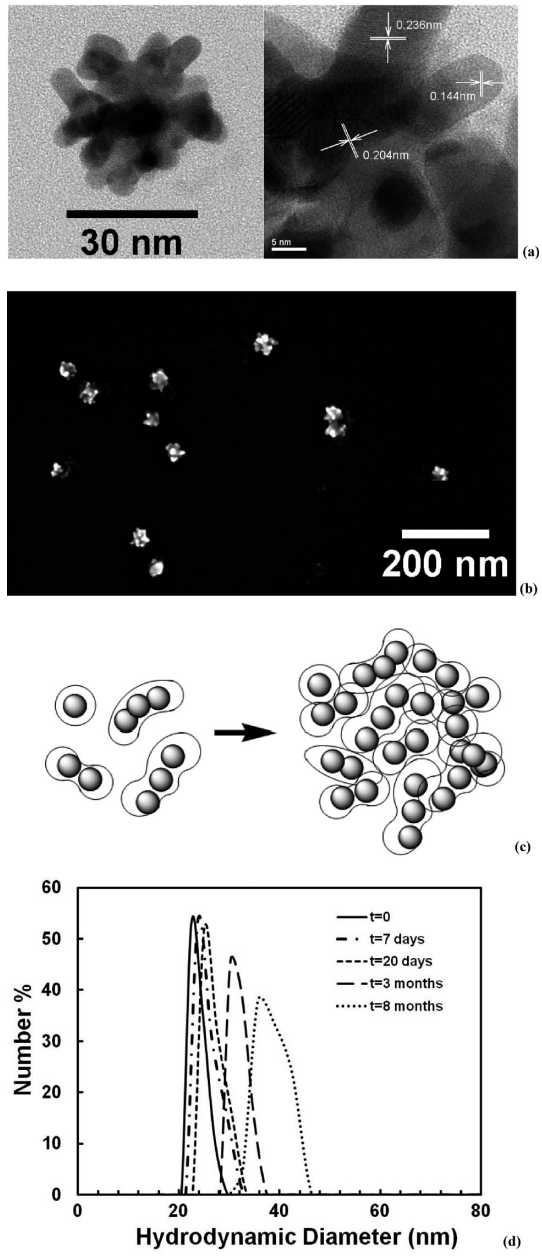

Figure 1. Size, shape, and colloidal stability of nanoclusters (nanoroses) in deionized (DI) water. (a) High-resolution transmission electron microscopy (TEM) images on an ultrathin carbon film substrate reveal an open nanocluster of iron oxide@Au primary core−shell particles. The most prevalent lattice spacing is found to be 0.236 nm for the (111) plane of Au. The (200) and (220) planes are also indicated. (b) Scanning electron microscopy (SEM) image of dried nanoroses on silicon wafer. (c) Schematic of nanocluster of gold-coated iron oxide primary particles. (d) Hydrodynamic diameter in water from dynamic light scattering starts at 25 nm, and the small change in size up to 8 months at 4 °C indicating high colloidal stability.

kinetic control of the cluster size with a relatively low polydispersity shown by dynamic light scattering (DLS) (Figure 1d). The small hydrodynamic diameter of the nanorose in DI water ranged from 23 ± 3 and 34 ± 2 nm over seven separate experiments (Table S1 in Supporting Information). The relatively low polydispersities of these clusters are also evident by SEM (Figure 1b). Diameters changed relatively little, with an average of only 33 nm over 3 months and 39 nm in 8 months, as shown in Figure 1d. Thus, the iron oxide cores helped prevent growth of gold domains, and the dextran and PVA provided effective steric stabilization. The total polymer concentration was only 12% according to thermal gravimetric analysis (TGA), in contrast with larger amounts typically needed in block copolymer templated clusters.[20] In contrast, aggregation of gold nanoparticles by variation of surface charge in a recent study led to large micrometer-sized 3D assemblies with NIR absorption.[27]

A variety of measurements indicate that the oligomeric domains that formed the nanoclusters in Figure 1a contained primary iron oxide cores, as depicted schematically in Figure 1c. An energy-dispersive X-ray spectroscopy (EDS) line scan across the particle shows that Fe was present throughout the cluster diameter (Figure 2). This observation is consistent with the hydroxylamine seeded growth of gold on the iron oxide surface rather than that of pure gold particles. EDS measurements of 20 nanorose particles indicate that the Au/Fe mass ratio varied from 5:1 to 9:1, as shown in Figure 2. Smaller ratios of 3:1 to 4:1 were determined from flame atomic absorption spectroscopy (FAAS) as a consequence of the excess iron oxide particles (without gold coatings) in the dispersion, which were also seen by TEM in the very light particles near the nanorose surfaces in Figure 1a. If all of the iron oxide particles were coated with a uniform gold shell, the thickness for a 1:10 Au/Fe ratio would be less than 0.2 nm, which would not be possible. The gold nuclei grew on only a fraction of the iron oxide particles, and then further growth of gold was favored on these Au sites. The nucleation of gold took place over a relatively small time period, given the relatively low polydispersity in the final cluster size. The calculated number of primary iron oxide particles for a 35 nm nanorose was approximately 70, from the molar Au/Fe ratio determined by EDS and the assumption that the occupied volume within an effective spherical nanorose (with diameter equivalent to the end-to-end distance) was approximately 50% (Supporting Information).

Optical and Magnetic Properties in Solution. The broad NIR absorbance of a colloidal nanorose dispersion shown in Figure 3 is relevant to tissue imaging and light-based therapy and drops only 5% at 800 nm from the maximum at 730 nm. Colloidal and optical stability of the nanorose may be attributed to prevention against growth or collapse of the gold domains by the iron oxide cores and polymer stabilizers for both the primary domains and the external surfaces of the clusters. For a dispersion with 32 μg Au/mL, as determined by FAAS in Figure 3a, the extinction coefficient at the maximum absorbance (730 nm) was 0.025 $cm^2/\mu g$ Au. The original dispersion was diluted to this concentration to obtain an absorbance maximum in the range of 0.4 to 1.0 As-

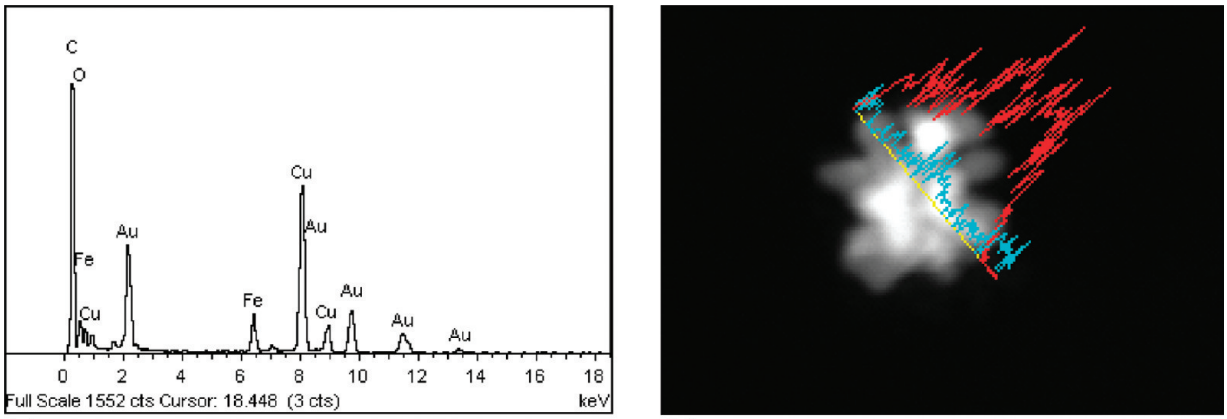

Figure 2. Energy-dispersive spectroscopy area scan and line scan coupled with STEM from one nanorose. STEM and EDS were performed on a field emission JEOL2010F transmission electron microscope equipped with an Oxford INCA EDS system. EDS line scan was performed with the microscope in STEM mode at 200 kV accelerating voltage. C and Cu peaks are from TEM sample grid (Cu) and ultrathin carbon substrate. Red intensity is from Au, and blue intensity is from Fe.

suming that gold occupies 50% of the volume of a nanorose with an end−end distance based on Figure 1a, we found that the dispersion in Figure 3a contained 10^{10} nanoroses per mL and thus a particle extinction cross section of $\sigma_{755nm} \sim 10^{-14}$ m^2. Similar particle cross sections were observed for nanocages, nanorods, and nanoshells.[12,28] The nanorose extinction cross section at 755 nm is 6 orders of magnitude larger than that of freshly prepared indocyanine green dissolved in NaCl aqueous buffer solution (1×10^{-20} m^2 at 778 nm), which has been investigated as a NIR dye for laser photothermal therapy.[29,30]

A further examination of the nanorose shape will now be used to explain the marked red shift in the SPR from 532 nm for a single spherical gold particle. For a single core−shell particle of gold on silica, the thickness of the shell to the core diameter must be in the range of 5% to shift the SPR to 900 nm, according to Mie theory.[31,32] For an average Au coating thickness of 0.7 on 5 nm diameter Fe_3O_4, the experimental SPR maximum shifted only to 600 nm, consistent with the above theoretical prediction.[25] Small red shifts were also observed for 1 nm gold shells on 10 nm diameter Fe_3O_4.[33] For our 5 nm iron oxide cores, a ~0.3 nm shell thickness would be required for an absorbance at 900 nm. Such thin shells of Au on iron oxide have not been reported. In our study, thin gold layers with an average thickness of ~1 to 2.5 nm were observed. A uniform shell of this thickness on a single 5 nm iron oxide core would be too thick to produce this large SPR red shift.[8,34] Instead, the red shift was caused by (1) collective responses of the electrons in the gold coatings on the closely spaced primary particles within the clusters and (2) asymmetry in the thickness of the gold coatings on each particle. An analogous type of red shift has been observed for multiple spherical gold particles in close proximity.[14,31,35] In Figure 1a, short oligomers of primary particles (subclusters) are evident in the shape of relatively high aspect ratio rods or bent rods containing kinks where the particles touch, as indicated in the schematic in Figure 1c. The high aspect ratio of these rods contributes to the SPR red shift more strongly than in the case of a dense spherical cluster composed of uniformly spaced primary particles.[28,31] The close approach of the primary particles coated with dextran is favored by the very low volume fraction of hydrated dextran in the shell (see Supporting Information) of 24% in the original iron oxide particles. A red shift would also be pro-

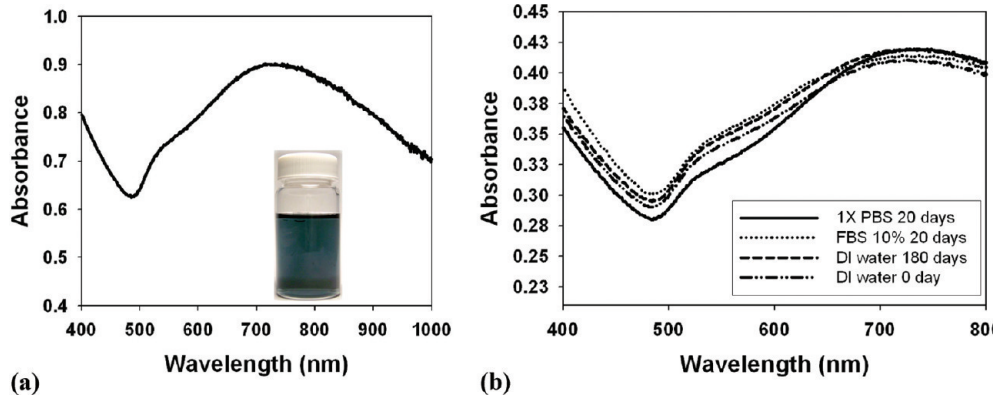

Figure 3. UV−vis−NIR absorbance spectra of colloidal nanorose dispersions in various media. (a) Blue dispersion in the inset indicates a strong absorbance in the NIR region for 32 μg/mL gold, as quantified by the spectra with 1 cm path length. (b) Similar strong NIR absorbance was observed in DI water, 1× PBS solution, and a DMEM supplemented with 10% FBS cell culture media, which was stable for ~180 days storage at 4 °C. The optical stability was consistent with the small change in size according to DLS in Figure 1d.

duced by differential thickness of the shells on a given particle at various locations on the surface, as has been observed for nanoeggs and nanocups with off-centered cores.[26,36] This shift results from reduced symmetry of the interactions between plasmon modes. The very thin shells in the nanorose primary particles are likely to exhibit these types of eccentric geometries, although distinguishing between the iron oxide and gold is difficult for the complex cluster geometry.

A knowledge of the contribution of absorption *versus* scattering for the nanoclusters is important for understanding various optical imaging applications. A direct optical properties measurement technique was used to measure the absorption and scattering cross section of the nanorose dispersion with an integrating sphere.[37,38] Absorption coefficient and scattering coefficient were computed using eqs 1 and 2:

$$\mu_a = \frac{1}{x}\frac{S_{a0} - S_a}{S_{a0}} \quad (1)$$

$$\mu_s = \frac{1}{x}\frac{S_s}{S_{s0}} \quad (2)$$

where x is the sample thickness (80 μm) and S_{a0} and S_a are the measured absorption radiant power with DI water and nanorose solution, respectively. The absorption cross section is given by μ_a divided by the number density. Samples were prepared at six nanorose concentrations (385, 193, 96, 77, 39, and 26 μg Au/mL) with corresponding nanorose number densities of 1.2×10^{11}, 0.6×10^{11}, 0.4×10^{11}, 0.24×10^{11}, 0.12×10^{11}, and 0.08×10^{11} nanoroses/mL, respectively. For these concentrations, the absorption coefficient $\mu_a = 29.3$, 19.2, 10.3, 7.6, 4.2, and 2.9 cm^{-1} and the corresponding averaged absorption cross section $\sigma_a = (3.1 \pm 0.5) \times 10^{-14}$ m^2 were computed according to the six nanorose concentrations. Data suggest the scattering cross section (σ_s) is much smaller than the absorption cross section and beyond the sensitivity of measurements. According to Mie theory, the contribution from absorption relative to scattering increases for spheres as the diameter decreases and for nanoshells as the shell thickness decreases, consistent with our results for extremely small particles and thin gold shells.[28] Experimentally, this behavior has been observed for nanocages with a decrease in the particle size.[12] The strong absorption for very small gold domains is beneficial for imaging techniques such as optical coherence tomography and photoacoustic spectroscopy and for photothermal therapy.[7,8,39]

The normalized saturation magnetization at 300 K was 34 emu/g Fe_3O_4 as measured by a superconducting quantum interference device (SQUID) magnetometer (Quantum Design MPMS), as shown in Figure 4a. To convert from magnetization per total mass of particles

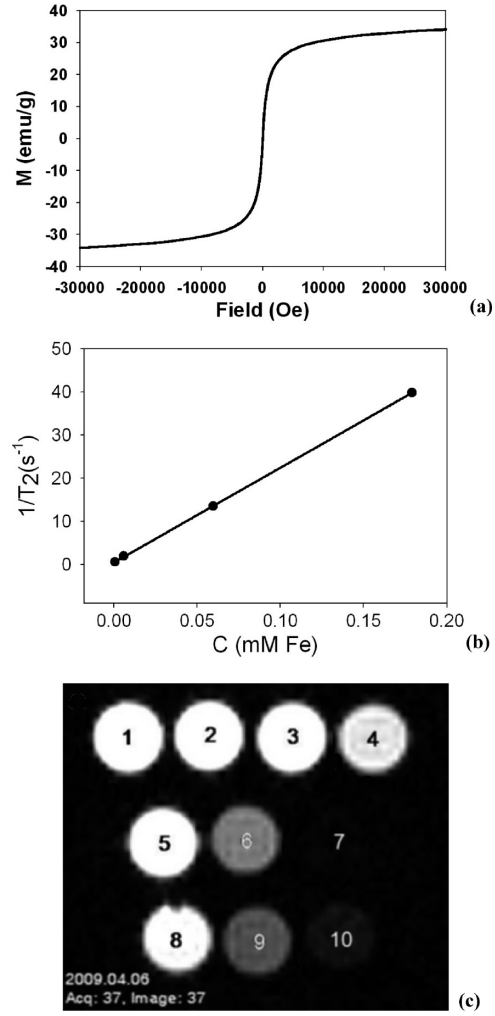

Figure 4. (a) Normalized nanorose magnetization per gram of Fe_3O_4 *vs* field strength at 300 K. (b) Reciprocal spin−spin relaxation time T_2 *vs* iron concentration in water. Relaxivity value (r_2) of 219 mM^{-1} s^{-1} was determined from the slope. (c) T_2-weighted magnetic resonance fast spin echo images of syringes containing solutions of Feridex I.V. and nanorose in phosphate buffer saline and blood. Concentrations are based upon iron content. Tube: (1) saline; (2−4) 1.75, 17.5, and 52.5 μg Fe/mL Feridex in saline; (5−7) 1.75, 17.5, and 52.5 μg Fe/mL nanorose in saline; (8−10) 1.75, 17.5, and 52.5 μg Fe/mL nanorose in blood. At equivalent iron concentrations, these results are consistent with nanorose inducing shorter relaxation time than Feridex.

to a basis of per mass of Fe_3O_4, the mass ratio of Au/Fe was 3:1, as determined by FAAS, and the polymer amount was 12% as determined by TGA. The magnetization approached the value of 39 emu/g Fe_3O_4 (54 emu/g Fe) for the original 5 nm iron oxide nanoparticles, indicating little interference from the gold coating. For single-crystal Fe_3O_4, the saturation magnetization increased with an increase in size from 4 to 12 nm, as the loss from the surface effect decreased.[40,41] In our case, the spins in adjacent primary iron oxide particles were not close enough to raise the mass magnetization over that of the individual primary particles, as has been observed for sub-100 nm polymer-coated iron oxide nanoparticles.[42]

The r_2 transverse relaxivity measured with the 3.0 T MRI was 219 mM^{-1} s^{-1} (Figure 4b), comparable to the high value obtained for solid iron oxide spheres formed in organic solvents at elevated temperatures.[40] This r_2 value was over twice those typically obtained for iron oxide spherical particles, including Feridex I.V. (AMAG Pharmaceuticals, Inc.) approved for clinical use by the FDA.[40] Water protons experience an inhomogeneity in the external field produced by the local magnetic field gradient about the superparamagnetic iron oxide particles.[43] This gradient produces dephasing of the proton spins and increases the r_2 relaxation rate. The r_2 increases upon nanoparticle assembly into clusters that raise the cross-sectional area.[41,43] For single-crystal Fe_3O_4 nanoparticles, the increase in mass magnetization with an increase in size from 4 to 12 nm produces an increased r_2.[40] However, the relationship between the cluster geometry and r_2 is not well-understood theoretically for complex cluster geometries, as in the case of nanorose.[23,41,43,44] The high r_2 is favored by the porous structure of the nanoclusters and the thin gold coatings (<3 nm) that result in short distances between iron oxide surfaces and water molecules, which favor high local inhomogeneities in the magnetic field. For more typical iron oxide particles with gold shells thicker than 5 nm, the r_2 is about an order of magnitude lower.[16] It is also enhanced by the iron oxide particles without gold coatings associated with the clusters that pack closely together. The higher r_2 value for the nanorose relative to Feridex I.V. is manifested in improved negative contrast (lower T_2 values and darker images) in MR imaging, as shown in Figure 4c. Furthermore, the images become darker with an increase in nanoparticle concentration.

The nanorose clusters exhibit intense single and multifunctionality whereby the NIR absorbance and magnetic relaxivity increase markedly upon assembly of the cluster, relative to the initial ~5 nm primary particles. Similarly sized virus capsids in nature are also assemblies of ~5 nm particles (proteins) with intense functionality. In the case of virus capsids and templated synthetic nanoclusters, the clusters are highly ordered assemblies of nanoparticles, in contrast with the disordered nanorose.[20] For the nanorose, the disorder makes the cluster design and synthesis simpler and more adaptable because templating agents such as block copolymers, DNA, or proteins are not needed.

Cell Targeting, Imaging, and Photothermolysis. Macrophages are implicated in every stage of atherosclerosis from lesion initiation to plaque rupture and clinical presentation.[45,46] Tumor-associated macrophages also play an important role in promoting tumor growth, invasion, metastasis, and angiogenesis.[47−50] Macrophage targeting *via* administration of NIR-sensitive nanoparticles may enhance diagnosis and therapy for both these conditions. The targeted uptake of nanorose for enhancement of cellular imaging and also photothermolysis was investigated with primary peritoneal macrophages, which were isolated from C57/BL6 mice. These mice can develop the M2 phenotype associated with cancer.[51] We incubated 10^5 cells with nanorose in culture media for 24 h. In Figure 5, for 10 μg Au/mL dose, the brown domains inside the cell under phase contrast mode (40× objective lens) show an extensive distribution of nanoroses. In the dark field mode, 610−800 nm light was reflected by nanorose-labeled macrophages producing strong contrast, relative to the unlabeled control.

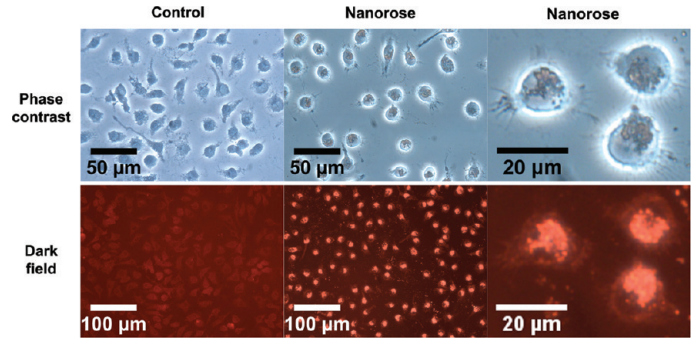

Figure 5. Phase contrast and dark field microscopy images of macrophages labeled with nanorose in DMEM supplemented with 10% FBS media. The left panels do not include nanoroses. The middle and right panels at two different levels of magnification include nanoroses at 10 μg Au/mL. The dark field reflectance images (20× objective lens) included a 610 nm long pass filter in the path of illumination. All images were recorded with Xe lamp illumination.

A high optical contrast for labeled macrophages for a relatively low nanorose dose requires high cellular uptake and a strong absorbance cross section per nanorose cluster. As shown in Figure 6 for a concentration of only 30 μg Au/mL culture media, the uptake reached saturation at 10^4 nanoroses per cell for 10^5 macrophages. This uptake level is far above the minimum value of a few hundred required to discriminate between nanorose-labeled *versus* unlabeled macrophages under dark field microscopy with a 40× objective lens. The optical densities, $\log_{10}(I_0/I_{sample})$, of nanorose-loaded macrophages were collected with a PARISS hyperspectral imaging instrument (Lightform, Inc.) in transmission bright field mode with a halogen illumina-

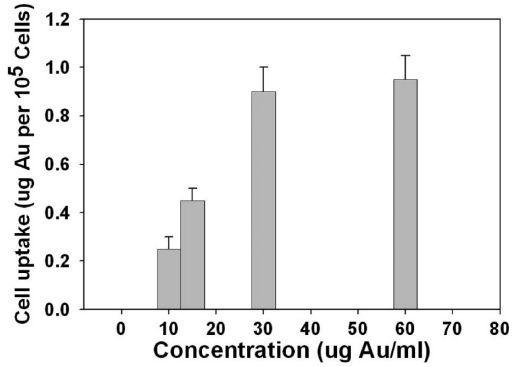

Figure 6. Strong uptake of nanoroses by macrophages as determined by flame atomic absorption spectroscopy for 10^5 cells.

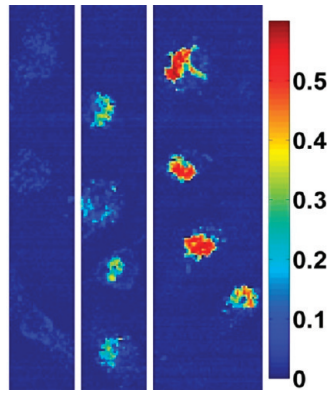

Figure 7. Hyperspectral microscopy images illustrating strong absorbance at 755 nm for nanorose in macrophages *in vitro*. The legend provides a color code for the optical density values up to 0.6. From left to right, macrophages were incubated with nanoroses (0.0, 1.0, and 10 μg Au/mL media) for 24 h. Area averaged spectra on the same macrophages are shown in Supporting Information Figure S3.

tor (see Supporting Information). For the three nanorose concentrations indicated, 10^5 macrophages were incubated with nanoroses in DMEM culture medium supplemented with 10% FBS for 24 h (Figure 7). A pronounced increase in absorbance was observed over this concentration range, reaching 0.6, indicating the potential for high NIR contrast for optical imaging despite the relatively low nanorose dose.

The high NIR absorbance of the nanorose may benefit photothermal cancer therapy of tumors containing macrophages. The macrophages were cultured in phenol-free DMEM plus 10% FBS media at 37 °C in 5% CO_2 for 24 h before they were treated with nanoroses. In Figure 8, a monolayer of macrophages, which had engulfed nanoroses, was irradiated with a Q-switched alexandrite laser for a single 755 nm pulse of 50 ns duration and a 2 mm spot size providing a fluence of 18 J/cm^2. A HgCdTe infrared detector was used to measure the temperature after irradiation. Immediately after irradiation, Figure 8c shows a 0.7 °C increase over the 2 mm spot, indicating strong absorbance by the nanorose. The measured temperature increase represents an average value over the effective aperture at the air−cell interface. The actual temperature increase immediately adjacent to the small nanorose cluster is substantially larger and localized to a small volume. Outside yet close to the edge of the beam, macrophage cells in a bright field image (Supporting Information Figure S4) were stained brown, indicating TUNEL positivity caused by heating. Identical laser irradiation without nanorose results in no change in phenotype and absence of TUNEL positivity. This positivity with nanorose present may suggest apoptosis, which would be of interest in the treatment of atherosclerosis and other macrophage-associated pathologies.

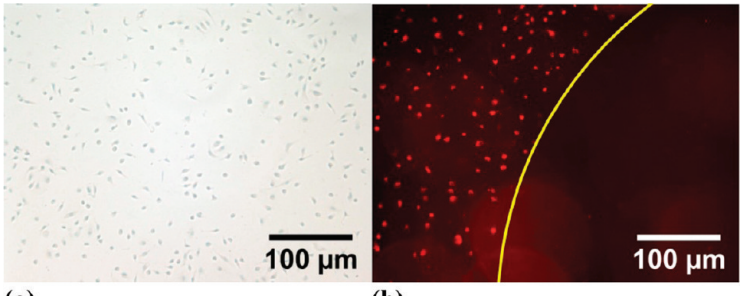

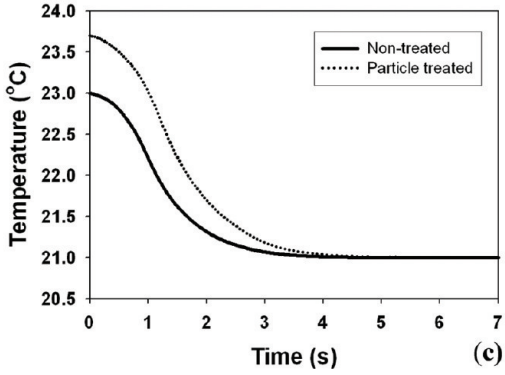

Figure 8. Laser photothermolysis of macrophages *in vitro* with a single 50 ns pulse at 755 nm at a fluence of 18 J/cm^2. (a) After irradiation without nanorose, a bright field image with TUNEL staining indicates the macrophage membranes were intact. (b) After irradiation with nanorose, a dark field image shows a zone of macrophage photothermolysis coincident with the laser beam. (c) Radiometric temperature following pulse radiation over an area with 2 mm diameter.

Macrophage Cell Uptake Specificity. To evaluate the specificity of targeting of macrophage cells associated with atherosclerosis, the uptake of nanorose among three major cell types including macrophages, endothelial cells (EC), and smooth muscle cells (SMC) in the aorta was evaluated. All cell lines were first allowed to reach confluence in LabTek chamber slides (Supporting Information). Each cell type was then treated with 1 μg/mL nanorose in 10% FBS DMEM/endothelial cell (EC) growth media for 4 h. Control samples were not treated with nanorose. After 4 h of treatment, all samples were washed three times with PBS and fixed in 5% formaldehyde.

According to Figure 9, the dextran-coated nanorose particles were taken up much more aggressively by macrophages than either aortic smooth muscle cells or aortic endothelial cells. The structure of the cells is shown in greater detail by dark field imaging without a filter in the Supporting Information (Figure S5). This specificity is the basis for the following imaging experiments in macrophage cells associated with an atherosclerotic rabbit aorta.

Atherosclerotic Rabbit Aorta Imaging. Macrophage targeting and imaging may be used to enhance diagnosis and therapy of atherosclerosis. We performed *in vivo* cellular imaging of atherosclerosis in a double-balloon-injured fat-fed rabbit model known for high prevalence of macrophages (Figure 10).[52] We injected the injured New Zealand white rabbit (age = 6 months, weight = 3.3 kg) intravenously with 12 cc of a colloidal dispersion of nanoroses (1.37 mg Au/kg body weight). The *in vivo* intravenous dose given to the rabbit is comparable to the

currently FDA approved value of 100 mg for a single injection of gold sodium thiomalate (per a 70 kg human body) used in the treatment of rheumatoid arthritis.[53] Three days following gold nanorose injection, the rabbit was euthanized and aortic specimens were harvested. The plaque-based macrophages engulf nanorose following intravenous injection, as demonstrated *via* co-localization of macrophage immunohistochemistry (RAM-11 positive) and nanorose identified with both dark field microscopy and hyperspectral imaging (see Figure 10 legend for details). Nanoroses engulfed by the macrophages retain their strong NIR absorbance seen in solutions and cell culture (Figures 3 and 7). High nanorose uptake and absorbance, along with the absence of NIR reflective components of native rabbit aorta, provide high contrast between macrophages and surrounding tissue.

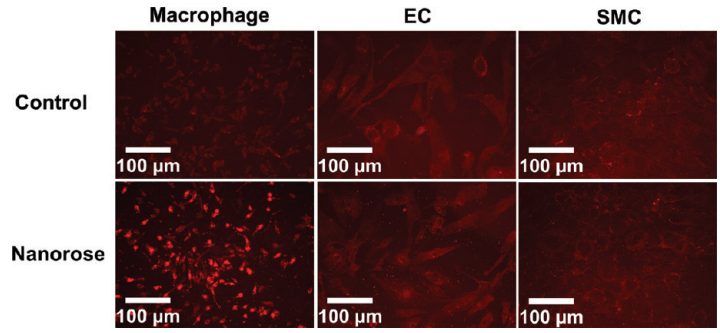

Figure 9. Specificity of nanorose into macrophages *versus* aortic endothelial cells and aortic smooth muscle cells by dark field microscopy with a 610 nm long pass filter. The top row is a control without incubation of nanorose. In the bottom row, the bright spots indicate NIR reflectance from nanorose in macrophage cells, at wavelengths above 610 nm, which is not evident for the other cells.

CONCLUSION

Strong NIR and magnetic functionality were loaded into very small ~30 nm nanoclusters that were relatively stable for 8 months. The nanoclusters were formed by kinetic assembly of Au/iron oxide nanocomposite building blocks with only a small amount of polymeric stabilizers. The closely spaced and asymmetric thin gold coatings on the primary particles and porosity of the nanoclusters favor high NIR absorbance as a result of collective responses of the electrons and reduced symmetry of the interactions between plasmon modes. The large degree of empty space in the clusters is beneficial for further addition of adsorbed or conjugated (onto gold) drugs, antibodies, and aptamers.[15] The primary components of the particles, iron oxide, Au, dextran, and poly(vinyl alcohol) (PVA), are acceptable for administration to humans, without the need for toxic surfactants or toxic metals. The small size of the nanoclusters and the dextran surface coating are shown to facilitate high uptake by macrophages, which contain dextran receptors.[6] The high uptake and intense NIR absorbance are shown to provide high NIR contrast in dark field and hyperspectral microscopy, both in cell culture and an *in vivo* rabbit model of atherosclerosis. A single 50 ns laser pulse at 755 nm is sufficient for photothermal destruction of nanocluster-laden macrophages. Small and stable nanoclusters of nanocomposite primary particles with strong multifunctionality, designed by this general approach, will offer broad opportunities for cellular imaging and altering cell biology for the treatment of diseases such as atherosclerosis and cancer.

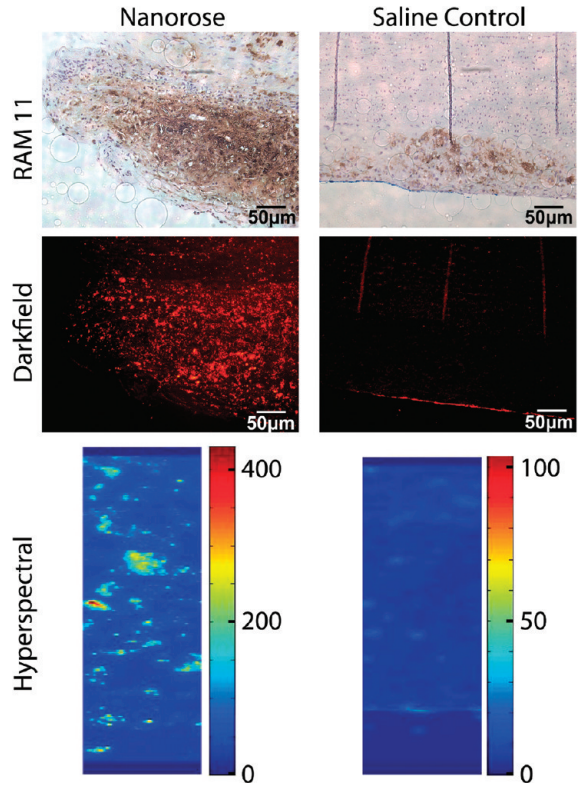

Figure 10. Histological sections of atherosclerotic rabbit aorta. Leftmost images are double-balloon-injured aorta after intravenous injection with nanorose; rightmost images are from a saline-injected control rabbit. RAM 11 stain (brown color) shows macrophages are present in both rabbits. Dark field microscopy with a 610 nm long pass filter shows nanorose in the double-balloon-injured aorta only (bright red reflections). Hyperspectral images (integrated reflectance intensities of light between 610 and 800 nm) show nanorose (yellow-red intensities) within the macrophages (blue intensities) in the double-balloon-injured aorta.

METHODS

Synthesis of Iron Oxide Dispersion. The iron oxide nanoparticles were synthesized by using a modified method of Shen *et al.*[54] Fifteen milliliters of dextran aqueous solution (15% w/w) was titrated with 4 mL of NH_4OH (>25% w/w) to pH 11.7. The alkali-treated dextran solution was heated in a flask with magnetic stirring to 25 °C in a water bath. Five milliliters of freshly prepared 0.75 g of $FeCl_3 \cdot 6H_2O$ and 0.32 g of $FeCl_2 \cdot 4H_2O$ aqueous solution was gradually injected into the alkali-treated dextran solution after passing through a hydrophilic 0.2 μm filter. The black suspension was

stirred for 0.5 h. The subsequent mixture was centrifuged at 10 000 rpm for 20 min to remove the aggregates. The supernatant was decanted and dialyzed against DI water for 24 h. For a dialysis bag (Spectra/Pro 7, Spectrum Laboratories Inc.) with 25 kDa molecular weight cut off, heavy metal ions, excess salts, ammonium, and unbound dextran molecules were removed from the particle dispersion. To concentrate the dispersions and further remove free dextran from the particles, a centrifugal filter device (Ultracel YM-30, Millipore Co.) was used with a relative centrifugal force of 1500*g*. The size of the iron oxide nanoparticles in this supernatant measured by HRTEM was 5.2 ± 0.8 nm, and the pH was 7.3. The concentration of iron oxide from FAAS was 14.6 mg Fe/mL. After dilution to 0.1 mg/mL Fe, DLS gave an average hydrodynamic diameter of 14 nm at 25 °C (see Supporting Information Figure S1).

Nanorose Growth and Purification. To synthesize the nanorose, 0.1 mL (14.6 mg Fe/mL) of 5 nm dextran-coated iron oxide nanoparticles was dispersed in 8.9 mL of DI water, and 100 μL of 1% hydroxylamine seeding agent was added; 0.5 g of dextrose was used as a more mild reducing agent compared with sodium citrate that was used previously.[24] Before starting the Au precursor addition, 20 μL of 7% NH_4OH solution was added to the iron oxide dispersion to tune the pH to 9.0. A 100 μL aliquot of 6.348 mM $HAuCl_4$ aqueous solution was added to the stirred dispersion. After 10 min, a second 100 μL aliquot was added. This procedure was repeated two more times for a total of 400 μL of $HAuCl_4$. A gradual change in color from brown to dark brown occurred during the four aliquot additions, and the pH decreased to 7.0. The dense gold-coated iron oxide particles were separated from the less dense uncoated particles by centrifugation at 6000 rpm for 6 min; 1.6−2.3% iron oxide nanoparticles from the original reaction was incorporated in the nanorose precipitate as determined by FAAS. After decanting the supernatant, we re-dispersed purified gold-coated iron oxide nanorose in DI water. Dialysis bags were used to purify the nanoroses further against DI water for 24 h, and the dispersions were sterilized by passage through a 0.45 μm pore size Nylon filter. The purified particles were then concentrated by centrifugal filter devices (Ultracel YM-30, Millipore Co.) to 700 μg Au/mL in a total volume of 0.1 mL. The final product appeared dark blue in color to the unaided eye. To improve the steric stabilization of the nanorose clusters, 40 μL of 2% poly(vinyl alcohol) MW 22 000 was added to the dispersions. After 8 months storage, a small portion of the settled particles was redispersible by manual shaking without any visible aggregates.

Dynamic Light Scattering. Dynamic light scattering analysis was performed in triplicate on a custom-built apparatus (scattering angle: 90°), and the data were analyzed using a digital autocorrelator (Brookhaven BI-9000AT) and a non-negative least-squares (NNLS) routine (Brookhaven 9KDLSW32).[55] The dispersion concentration was 0.02−0.04 mg Au/mL, which gave a measured count rate of approximately 300−400 kcps. All dispersions were filtered through a 0.2 μm filter and probe-sonicated for 2 min prior to measurement.

Determination of Absorption and Scattering with an Integrating Sphere. A lens coupled fiber optic laser (Opto Power, Inc.; Model FCTS/B) was used to irradiate a sample positioned inside an integrating sphere. The sample was positioned in a glass sample holder and consisted of two microscope slides displaced by 80 μm. The sample holder was positioned in the center of the integrating sphere and oriented perpendicular to the incident laser beam (3 W, 800 nm, CW mode). A power meter (Newport, Inc.; Model 1935-C) was placed at a port of the integrating sphere oriented perpendicular to the laser beam. For absorption coefficient (μ_a) measurement, the radiant power was measured with the sample holder containing DI water and nanorose solution. The directly transmitted beam through the sample holder was contained within the integrating sphere and contributed to the measurement. For scattering coefficient (μ_s) measurement, the same procedure was followed except that the directly transmitted beam was allowed to exit the integrating sphere and did not contribute to the measurement.

***In Vitro* Magnetic Resonance Imaging.** All MRI experiments were performed with a 3.0 T clinical MRI instrument (Trio, Siemens Medical Solutions) with a circularly polarized, transmit-receive knee coil. The resonant frequency was 123.208591 MHz. The microscopic transverse relaxation time (T_2) was measured for various concentrations of nanorose particles by applying spin echo (SE) pulse sequences at room temperature with T_R = 2 s and increasing the echo time (T_E) for successive scans: T_E = 7, 14, 28, 56, 112, 224, 448, and 896 ms. Other parameters included the number of acquisitions (N_A) = 1, pixel resolution = 0.351 mm × 0.351 mm, bandwidth = 200 Hz/pixel, and section thickness = 2 mm. Following data collection, regions of interest (ROIs) were drawn, and the mean signal intensity in each tube was recorded. Nonlinear least-squares fitting was used to solve for T_2 as a function of iron concentration in millimolar. The relaxivity value (r_2 in mM^{-1} s^{-1}) for the nanorose dispersion was calculated using T_2 measurements done with a series dilution of colloidal suspension in water.

***In Vitro* Macrophage Photothermolysis Study.** For photothermolysis, 1 mL of culture media containing 1 μg of nanorose was incubated in each well of a dual chamber slide for 24 h followed by intensive 1× PBS washing to remove nonengulfed nanoparticles. The amounts of gold and iron in the engulfed nanorose were determined by FAAS. The macrophages were cultured for another 24 h after each laser treatment before staining and microscopy imaging. A Candela Alexlazr laser (Candela Corporation, Wayland, MA) with a wavelength of 755 nm was used to irradiate the slides. Radiometric temperature was measured by focusing the IR radiation with a parabolic mirror onto a HgCdTe infrared detector (Fermionics Corporation, Simi Valley, CA) with 11 μm cutoff wavelength. The measured voltage was calibrated to a temperature using a blackbody source.

Hyperspectral Microscopy. The Pariss hyperspectral system was coupled to a Leica microscope and measured the spectra of transmitted light at each pixel in an image, for illumination with a halogen lamp (300−780 nm). A single vertical section of the sample image was projected onto a prism through a 25 μm slit and a prism dispersed the one-dimensional image onto a two-dimensional Q-imaging Retiga EXi CCD detector, with spatial information encoded on one axis and spectral information on the orthogonal direction. The macrophage samples were laterally scanned *via* a piezoelectric stage to construct a three-dimensional hyperspectral data cube. A blank slide containing 1× PBS was used to acquire spectrum of the illumination lamp.

Atherosclerotic Rabbit Model. All experimental procedures were performed in accordance with protocols approved by the University of Texas Institutional Animal Care and Use Committee. Atherosclerotic plaques rich in macrophages were induced in New Zealand white rabbits by double-balloon injury and high cholesterol, high fat feeding as previously reported.[52] The tissue specimens were fixed in 10% formalin for 24 h, processed for histology, and embedded in paraffin. An aortic specimen from a control rabbit was prepared. The control rabbit (age = 6 months, weight = 3.3 kg) was fed and injured in the same way, but received 12 cc of saline without any nanorose.

Acknowledgment. This work was supported in part by a Veterans Administration Merit grant, the STC Program of the National Science Foundation under Agreement No. CHE-9876674, NIH (CA 103830), NIH RO1 EB008821-01, NIH Training Grant No. HL07446, and the Welch Foundation (F-1319). The authors gratefully acknowledge Candela Laser (Wayland, MA) for use of the Alexandrite laser.

Supporting Information Available: Reproducibility in nanorose size distribution; porosity of dextran in the shells about the iron oxide particle; estimation of number of particles per nanocluster; average optical density spectra in macrophages labeled with nanorose by hyperspectral microscopy; and laser vaporization of macrophages *in vitro*. This material is available free of charge *via* the Internet at http://pubs.acs.org.

REFERENCES AND NOTES

1. Ferrari, M. Beyond Drug Delivery. *Nat. Nanotechnol.* **2008**, *3*, 131–132.
2. Jiang, W.; Kim, B. Y. S.; Rutka, J. T.; Chan, W. C. W. Nanoparticle-Mediated Cellular Response is Size-Dependent. *Nat. Nanotechnol.* **2008**, *3*, 145–150.

3. Reddy, S. T.; Swartz, M. A.; Hubbell, J. A. Targeting Dendritic Cells with Biomaterials: Developing the Next Generation of Vaccines. *Trends Immunol.* **2006**, *27*, 573–579.
4. Wang, A. Z.; Bagalkot, V.; Vasilliou, C. C.; Gu, F.; Alexis, F.; Zhang, L.; Shaikh, M.; Yuet, K.; Cima, M. J.; Langer, R.; Kantoff, P. W.; Bander, N. H.; Jon, S.; Farokhzad, O. C. Superparamagnetic Iron Oxide Nanoparticle−Aptamer Bioconjugates for Combined Prostate Cancer Imaging and Therapy. *ChemMedChem* **2008**, *3*, 1311–1315.
5. Weissleder, R. Molecular Imaging in Cancer. *Science* **2006**, *312*, 1168–1171.
6. Jaffer, F. A.; Libby, P.; Weissleder, R. Molecular and Cellular Imaging of Atherosclerosis: Emergency Applications. *J. Am. Coll. Cardiol.* **2006**, *47*, 1328–1338.
7. Adler, D. C.; Huang, S.-W.; Huber, R.; Fujimoto, J. G. Photothermal Detection of Gold Nanoparticles Using Phase-Sensitive Optical Coherence Tomography. *Opt. Express* **2008**, *16*, 4376–4393.
8. Hirsch, L. R.; Stafford, R. J.; Bankson, J. A.; Sershen, S. R.; Rivera, B.; Price, R. E.; Hazle, J. D.; Halas, N. J.; West, J. L. Nanoshell-Mediated Near-Infrared Thermal Therapy of Tumors under Magnetic Resonance Guidance. *Proc. Natl. Acad. Sci. U.S.A.* **2003**, *100*, 13549–13554.
9. Loo, C.; Lowery, A.; Halas, N.; West, J.; Drezek, R. Immunotargeted Nanoshells for Integrated Cancer Imaging and Therapy. *Nano Lett.* **2005**, *5*, 709–711.
10. Huang, X.; El-Sayed, I. H.; Qian, W.; El-Sayed, M. A. Cancer Cell Imaging and Photothermal Therapy in the Near-Infrared Region by Using Gold Nanorods. *J. Am. Chem. Soc.* **2006**, *128*, 2115–2120.
11. Pissuwan, D.; Valenzuela, S. M.; Killingsworth, M. C.; Xu, X.; Cortie, M. B. Targeted Destruction of Murine Macrophage Cells with Bioconjugated Gold Nanorods. *J. Nanopart. Res.* **2007**, *9*, 1109–1124.
12. Skrabalak, S. E.; Chen, J.; Au, L.; Lu, X.; Li, X.; Xia, Y. Gold Nanocages for Biomedical Applications. *Adv. Mater.* **2007**, *19*, 3177–3184.
13. Sokolov, K.; Follen, M.; Aaron, J.; Pavlova, I.; Malpica, A.; Lotan, R.; Richards-Kortum, R. Real-Time Vital Optical Imaging of Precancer Using Anti-Epidermal Growth Factor Receptor Antibodies Conjugated to Gold Nanoparticles. *Cancer Res.* **2003**, *63*, 1999–2004.
14. Aaron, J.; Nitin, N.; Travis, K.; Kumar, S.; Collier, T.; Park, S. Y.; Jose-Yacaman, M.; Coghlan, L.; Follen, M.; Richards-Kortum, R.; Sokolov, K. Plasmon Resonance Coupling of Metal Nanoparticles for Molecular Imaging of Carcinogenesis *In Vivo*. *J. Biomed. Opt.* **2007**, *12*, 034007/1–034007/11.
15. Josephson, L.; Kircher, M. F.; Mahmood, U.; Tang, Y.; Weissleder, R. Near-Infrared Fluorescent Nanoparticles as Combined MR/Optical Imaging Probes. *Bioconjugate Chem.* **2002**, *13*, 554–560.
16. Larson, T. A.; Bankson, J.; Aaron, J.; Sokolov, K. Hybrid Plasmonic Magnetic Nanoparticles as Molecular Specific Agents for Mri/Optical Imaging and Photothermal Therapy of Cancer Cells. *Nanotechnology* **2007**, *18*, 325101/1–325101/8.
17. Aaron, J. S.; Oh, J.; Larson, T. A.; Kumar, S.; Milner, T. E.; Sokolov, K. V. Increased Optical Contrast in Imaging of Epidermal Growth Factor Receptor Using Magnetically Actuated Hybrid Gold/Iron Oxide Nanoparticles. *Opt. Express* **2006**, *14*, 12930–12943.
18. Yin, Y.; Alivisatos, A. P. Colloidal Nanocrystal Synthesis and the Organic−Inorganic Interface. *Nature* **2005**, *437*, 664–670.
19. DeVries, G. A.; Brunnbauer, M.; Hu, Y.; Jackson, A. M.; Long, B.; Neltner, B. T.; Uzun, O.; Wunsch, B. H.; Stellacci, F. Divalent Metal Nanoparticles. *Science* **2007**, *315*, 358–361.
20. Ofir, Y.; Samanta, B.; Rotello, V. M. Polymer and Biopolymer Mediated Self-Assembly of Gold Nanoparticles. *Chem. Soc. Rev.* **2008**, *37*, 1814–1825.
21. Boal, A. K.; Ilhan, F.; DeRouchey, J. E.; Thurn-Albrecht, T.; Russell, T. P.; Rotello, V. M. Self-Assembly of Nanoparticles into Structured Spherical and Network Aggregates. *Nature* **2000**, *404*, 746–748.
22. Lazarides, A. A.; Schatz, G. C. DNA-Linked Metal Nanosphere Materials: Structural Basis for the Optical Properties. *J. Phys. Chem. B* **2000**, *104*, 460–467.
23. Berret, J.-F.; Schonbeck, N.; Gazeau, F.; El Kharrat, D.; Sandre, O.; Vacher, A.; Airiau, M. Controlled Clustering of Superparamagnetic Nanoparticles Using Block Copolymers: Design of New Contrast Agents for Magnetic Resonance Imaging. *J. Am. Chem. Soc.* **2006**, *128*, 1755–1761.
24. Lyon, J. L.; Fleming, D. A.; Stone, M. B.; Schiffer, P.; Williams, M. E. Synthesis of Fe Oxide Core/Au Shell Nanoparticles by Iterative Hydroxylamine Seeding. *Nano Lett.* **2004**, *4*, 719–723.
25. Wang, L.; Luo, J.; Fan, Q.; Suzuki, M.; Suzuki, I. S.; Engelhard, M. H.; Lin, Y.; Kim, N.; Wang, J. Q.; Zhong, C.-J. Monodispersed Core−Shell Fe_3O_4@Au Nanoparticles. *J. Phys. Chem. B* **2005**, *109*, 21593–21601.
26. Knight, M. W.; Halas, N. J. Nanoshells to Nanoeggs to Nanocups: Optical Properties of Reduced Symmetry Core-Shell Nanoparticles Beyond the Quasistatic Limit. *New J. Phys.* **2008**, 10.
27. Basu, S.; Pande, S.; Jana, S.; Bolisetty, S.; Pal, T. Controlled Interparticle Spacing for Surface-Modified Gold Nanoparticle Aggregates. *Langmuir* **2008**, *24*, 5562–5568.
28. Jain, P. K.; Lee, K. S.; El-Sayed, I. H.; El-Sayed, M. A. Calculated Absorption and Scattering Properties of Gold Nanoparticles of Different Size, Shape, and Composition: Applications in Biological Imaging and Biomedicine. *J. Phys. Chem. B* **2006**, *110*, 7238–7248.
29. Urbanska, K.; Romanowska-Dixon, B.; Matuszak, Z.; Oszajca, J.; Nowak-Sliwinska, P.; Stochel, G. Indocyanine Green as a Prospective Sensitizer for Photodynamic Therapy of Melanomas. *Acta Biochim. Polonica* **2002**, *49*, 387–391.
30. Chen, W. R.; Adams, R. L.; Carubelli, R.; Nordquist, R. E. Laser-Photosensitizer Assisted Immunotherapy: A Novel Modality for Cancer Treatment. *Cancer Lett.* **1997**, *115*, 25–30.
31. Khlebtsov, B.; Zharov, V.; Melnikov, A.; Tuchin, V.; Khlebtsov, N. Optical Amplification of Photothermal Therapy with Gold Nanoparticles and Nanoclusters. *Nanotechnology* **2006**, *17*, 5167–5179.
32. Wang, H.; Goodrich, G. P.; Tam, F.; Oubre, C.; Nordlander, P.; Halas, N. J. Controlled Texturing Modifies the Surface Topography and Plasmonic Properties of Au Nanoshells. *J. Phys. Chem. B* **2005**, *109*, 11083–11087.
33. Xu, Z.; Hou, Y.; Sun, S. Magnetic Core/Shell Fe_3O_4/Au and Fe_3O_4/Au/Ag Nanoparticles with Tunable Plasmonic Properties. *J. Am. Chem. Soc.* **2007**, *129*, 8698–8699.
34. Pham, T.; Jackson, J. B.; Halas, N. J.; Lee, T. R. Preparation and Characterization of Gold Nanoshells Coated with Self-Assembled Monolayers. *Langmuir* **2002**, *18*, 4915–4920.
35. Kumar, S.; Harrison, N.; Richards-Kortum, R.; Sokolov, K. Plasmonic Nanosensors for Imaging Intracellular Biomarkers in Live Cells. *Nano Lett.* **2007**, *7*, 1338–1343.
36. Wang, H.; Brandl, D. W.; Nordlander, P.; Halas, N. J. Plasmonic Nanostructures: Artificial Molecules. *Acc. Chem. Res.* **2007**, *40*, 53–62.
37. Wilson, B. C.; Patterson, M. S.; Flock, S. T. Indirect *versus* Direct Techniques for the Measurement of the Optical Properties of Tissues. *Photochem. Photobiol.* **1987**, *46*, 601–608.
38. Patterson, M. S.; Wilson, B. C.; Wyman, D. R. The Propagation of Optical Radiation in Tissue. II: Optical Properties of Tissues and Resulting Fluence Distributions. *Lasers Med. Sci.* **1991**, *6*, 379–390.
39. Shah, J.; Park, S.; Aglyamov, S.; Larson, T.; Ma, L.; Sokolov, K.; Johnston, K.; Milner, T.; Emelianov Stanislav, Y. Photoacoustic Imaging and Temperature Measurement for Photothermal Cancer Therapy. *J. Biomed. Opt.* **2008**, *13*, 034024.

40. Jun, Y.-W.; Lee, J.-H.; Cheon, J. Chemical Design of Nanoparticle Probes for High-Performance Magnetic Resonance Imaging. *Angew. Chem., Int. Ed.* **2008**, *47*, 5122–5135.
41. Lee, J.-H.; Huh, Y.-M.; Jun, Y.-W.; Seo, J.-W.; Jang, J.-T.; Song, H.-T.; Kim, S.; Cho, E.-J.; Yoon, H.-G.; Suh, J.-S.; Cheon, J. Artificially Engineered Magnetic Nanoparticles for Ultra-Sensitive Molecular Imaging. *Nat. Med.* **2007**, *13*, 95–99.
42. Ditsch, A.; Laibinis, P. E.; Wang, D. I. C.; Hatton, T. A. Controlled Clustering and Enhanced Stability of Polymer-Coated Magnetic Nanoparticles. *Langmuir* **2005**, *21*, 6006–6018.
43. Perez, J. M.; Josephson, L.; Weissleder, R. Use of Magnetic Nanoparticles as Nanosensors to Probe for Molecular Interactions. *ChemBioChem* **2004**, *5*, 261–264.
44. Roch, A.; Gossuin, Y.; Muller, R. N.; Gillis, P. Superparamagnetic Colloid Suspensions: Water Magnetic Relaxation and Clustering. *J. Magn. Magn. Mater.* **2005**, *293*, 532–539.
45. Ross, R. Atherosclerosis—An Inflammatory Disease. *New Engl. J. Med.* **1999**, *340*, 115–126.
46. Libby, P. Inflammation in Atherosclerosis. *Nature* **2002**, *420*, 868–874.
47. Kimura, Y. N.; Watari, K.; Fotovati, A.; Hosoi, F.; Yasumoto, K.; Izumi, H.; Kohno, K.; Umezawa, K.; Iguchi, H.; Shirouzu, K.; Takamori, S.; Kuwano, M.; Ono, M. Inflammatory Stimuli from Macrophages and Cancer Cells Synergistically Promote Tumor Growth and Angiogenesis. *Cancer Sci.* **2007**, *98*, 2009–2018.
48. Allavena, P.; Sica, A.; Solinas, G.; Porta, C.; Mantovani, A. The Inflammatory Micro-Environment in Tumor Progression: The Role of Tumor-Associated Macrophages. *Crit. Rev. Oncol./Hematol.* **2008**, *66*, 1–9.
49. Biswas, S. K.; Sica, A.; Lewis, C. E. Plasticity of Macrophage Function During Tumor Progression: Regulation by Distinct Molecular Mechanisms. *J. Immunol.* **2008**, *180*, 2011–2017.
50. Nardin, A.; Abastado, J.-P. Macrophages and Cancer. *Front. Biosci.* **2008**, *13*, 3494–3505.
51. Bastos, K. R. B.; Alvarez, J. M.; Marinho, C. R. F.; Rizzo, L. V.; Lima, M. R. D. I. *J. Leukocyte Biol.* **2002**, *71*, 271–278.
52. Hyafil, F.; Laissy, J.-P.; Mazighi, M.; Tchetche, D.; Louedec, L.; Adle-Biassette, H.; Chillon, S.; Henin, D.; Jacob, M.-P.; Letourneur, D.; Feldman Laurent, J. Ferumoxtran-10-Enhanced MRI of the Hypercholesterolemic Rabbit Aorta: Relationship between Signal Loss and Macrophage Infiltration. *Arterioscler. Thromb. Vasc. Biol.* **2006**, *26*, 176–181.
53. Shaw, C. F., III. Gold-Based Therapeutic Agents. *Chem. Rev.* **1999**, *99*, 2589–2600.
54. Shen, T.; Weissleder, R.; Papisov, M.; Bogdanov, A., Jr.; Brady, T. J. Monocrystalline Iron Oxide Nanocompounds (Mion): Physicochemical Properties. *Magn. Reson. Med.* **1993**, *29*, 599–604.
55. Ryoo, W.; Webber, S. E.; Johnston, K. P. Water-in-Carbon Dioxide Microemulsions with Methylated Branched Hydrocarbon Surfactants. *Ind. Eng. Chem. Res.* **2003**, *42*, 6348–6358.